**Correspondence to:**
M. A. Clilverd, macl@bas.ac.uk

# Electron Precipitation From the Outer Radiation Belt During the St. Patrick's Day Storm 2015: Observations, Modeling, and Validation

**Mark A. Clilverd[1]** [ID], **Craig J. Rodger[2]** [ID], **Max van de Kamp[3]**, and **Pekka T. Verronen[3]** [ID]

[1]British Antarctic Survey (UKRI-NERC), Cambridge, United Kingdom, [2]Department of Physics, University of Otago, Dunedin, New Zealand, [3]Finnish Meteorological Institute, Helsinki, Finland

**Abstract** Recently, a model for medium-energy (30–1000 keV) radiation belt-driven electron precipitation (ApEEP) has been put forward for use in decadal to century-long climate model runs as part of the Climate Modelling Intercomparison Project, phase 6 (CMIP6). The ApEEP model is based on directly observed precipitation data spanning 2002–2012 from the constellation of low-Earth-orbiting Polar Operational Environmental Satellites (POES). Here, we test the ApEEP model's ability using its magnetic local time variant, ApEEP_MLT, to accurately represent electron precipitation fluxes from the radiation belts during a large geomagnetic storm that occurred outside of the span of the development data set. In a study of narrowband subionospheric very low frequency (VLF) transmitter data collected during March 2015, continuous phase observations have been analyzed throughout the entire St. Patrick's Day geomagnetic storm period for the first time. Using phase data from the U.K. transmitter, call-sign GVT (22.1 kHz), received in Reykjavik, Iceland, electron precipitation fluxes from $L = 2.8$ to 5.4 are calculated around magnetic local noon (12 MLT) and magnetic midnight (00 MLT). VLF-inferred >30-keV fluxes are similar to the equivalent directly observed POES fluxes. The ApEEP_MLT >30-keV fluxes for $L < 5.5$ describe the overall St. Patrick's Day geomagnetic storm-driven flux enhancement well, although they are a factor of 1.7 (1.3) lower than POES (VLF-inferred) fluxes during the recovery phase. Such close agreement in >30-keV flux levels during a large geomagnetic storm, using three different techniques, indicates this flux forcing are appropriate for decadal climate simulations for which the ApEEP model was created.

## 1. Introduction

One of the largest geomagnetic storms during solar cycle 24 occurred on 17 March 2015. Widely known as the St. Patrick's Day storm, the disturbance originated from a coronal mass ejection associated with a C9 solar flare which occurred at ~02 UT on 15 March 2015. A sudden storm commencement occurred at ~04 UT on 17 March due to the arrival of an interplanetary shock driven by the magnetic cloud (Wu et al., 2016). Elevated geomagnetic activity levels lasted throughout 17 and 18 March, with the geomagnetic activity index Ap peaking at levels of 179 nT, slowly subsiding thereafter. The storm period has been investigated for many geophysical effects including the sudden loss of relativistic electrons from the outer radiation belt during the early storm period (e.g., Baker et al., 2016 ; Shprits et al., 2017).

The evolution of outer radiation belt electron fluxes during large storms like the St. Patrick's Day storm involves a delicate balance between transport, acceleration, and loss processes (e.g., Glauert et al., 2018 ; Reeves et al., 2003). Gyro-resonant wave-particle interactions of electrons with very low frequency (VLF) waves have been shown to produce acceleration and loss within the radiation belt (Horne et al., 2016). Waves that occur outside of the plasmapause, such as VLF chorus, diffusively scatter electrons into the atmospheric loss cone as well as accelerate some to higher energies (e.g., O'Brien et al., 2003). Waves inside the plasmapause, such as VLF hiss, are associated with loss processes only (e.g., Meredith et al., 2006 ; Rodger et al., 2007). Other waves, such as electro-magnetic ion cyclotron waves, have also been linked to electron precipitation over a wide range of energies (e.g., Hendry et al., 2017).

Whatever the cause of the energetic electron precipitation (EEP) into the atmosphere, the generation of excess ionization at altitudes of 50–100 km affects radio communication conditions and creates odd hydrogen (HOx) and odd nitrogen (NOx) species through ion chemistry reactions (Verronen et al., 2005). Both

HOx and NOx species are able to catalytically destroy ozone (Brasseur & Solomun, 2005) and consequently alter the radiative and dynamic balance of the atmosphere (e.g., Seppälä et al., 2009; Andersson et al., 2014, Seppälä & Clilverd, 2014). Therefore, understanding the loss of electrons from the radiation belts during geomagnetic storms is important, not only for radiation belt dynamics, but also for understanding the effects of space weather on the climate system (Clilverd et al., 2016).

The St. Patrick's Day storm has been studied previously using VLF radio signals from man-made transmitters. Narrowband VLF signals from naval transmitters can be received subionospherically over long distances, but the phases of the received signals can vary, due to a combination of changes in the transmitter-receiver path length and variations in the electron density integrated along the path. Because of this, phase perturbations to quiet-day levels can provide information on the characteristics of EEP into the D-region of the ionosphere (Clilverd et al., 2010; Simon Wedlund et al., 2014). Gokani et al. (2019) studied short-term amplitude and phase perturbations on subionospheric paths at quasi-constant $L = 4$ in order to investigate the significance of relativistic electron precipitation into the atmosphere during the first few hours of the St. Patrick's Day 2015 storm. The technique used in this study is similar to that undertaken by Gokani et al. (2019), but here, it is applied to a much longer data set, requiring high transmitter phase stability. Maurya et al. (2018) studied a subionospheric path covering equatorial latitudes to show that VLF signal amplitudes were perturbed for ~10 days following the storm, although analysis showing decreased D-region electron densities suggested the presence of traveling ionospheric disturbances rather than electron precipitation.

Narrowband subionospheric VLF signals have been used to investigate the characteristics of EEP during other geomagnetic storms. Simon Wedland et al. (2014) showed that amplitude perturbations lasting 20 days occurred following a sequence of two geomagnetic storms in July and August 2010. Enhanced outer radiation belt electron precipitation fluxes over the range $L = 3$ to 7 with energies of 10 keV to several MeV were inferred using a technique that combined the amplitude perturbations of two closely located transmitters with similar frequencies. Single transmitter amplitude-only perturbations were converted to outer radiation belt electron precipitation fluxes over periods of ~100 days at a time by Clilverd et al. (2010) with subsequent improvements by Neal et al. (2015). These studies were limited to ~100-day summer-only periods because of the difficulty in reproducing the observed wintertime quiet-time amplitude levels using modeling by the Long Wave Propagation Code (LWPC) (Ferguson & Snyder, 1990). Without knowledge of the background electron density profile characteristics, it is difficult to accurately model the electron precipitation characteristics. Studies are preferentially limited to amplitude-only analysis much of the time, due to the difficulties in determining if observed phase changes are due to geophysical, transmitter, or receiver effects (Clilverd et al., 2009).

Efforts to determine quiet-time D-region electron density profile characteristics over a range of latitudes, including the Arctic region, have been undertaken. This is modeled through the Wait profile (Wait & Spies, 1964). Using high quality, absolute phase, multipoint measurements close to and far from individual transmitters, the nondisturbed quiet-time D-region reference height ($H'$) and sharpness (beta) parameters of the Wait profile have been found for low latitudes (Thomson et al., 2014), midlatitudes (Thomson et al., 2017), and high latitudes (Thomson et al., 2018). However, at the higher latitudes associated with the magnetic field-line footprints of the outer radiation belt, this has only been achieved for summertime, daylight conditions. At the current time, the characteristics of the high-latitude nighttime D-region electron density that can explain observed VLF subionspheric propagation signal levels remain an outstanding question.

A model for 30–1000 keV radiation belt-driven EEP, based on satellite data, has been put forward for use in climate models (van de Kamp et al., 2016). The EEP model is based on electron precipitation data spanning 2002–2012 from the constellation of low-Earth-orbiting Polar Operational Environmental Satellites (POES) (Rodger et al., 2010). The inclusion of EEP into the Climate Modelling Intercomparison Project, phase 6 (CMIP6) (Matthes et al., 2017) required an EEP model that was binned in geomagnetic latitude, and geomagnetic activity (the Ap index), but was zonally averaged, and had a time resolution of 1 day. The model is referred to as ApEEP. Multiple earlier studies into the atmospheric and climate impacts of EEP have made use of directly observed POES EEP fluxes (Andersson et al., 2014; Newnham et al., 2018; Orsolini et al., 2018), albeit binned by time and latitude. The ApEEP model is more suitable for long climate runs than the direct POES EEP flux approach (Andersson et al., 2018), as the latter is limited to the time period of
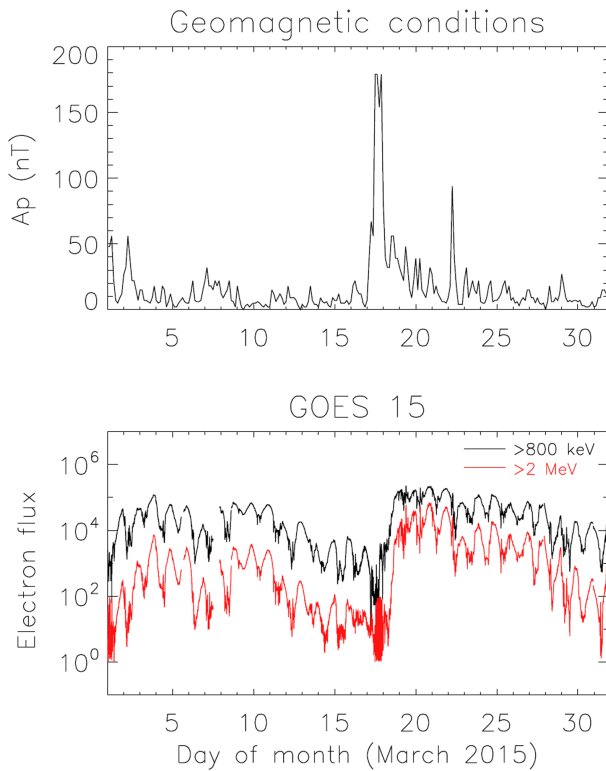
**Figure 1.** A summary plot of the geomagnetic conditions and GOES-15 geostationary trapped electron flux variations (el. $\text{Cm}^{-2}\,\text{s}^{-1}\,\text{sr}^{-1}$) during the disturbed period in march 2015.

those direct observations. The ApEEP model incorporated in the CMIP6 project is suitable for climate modeling approaches back to 1850 and can be used in future climate model runs, using statistically predicted Ap values (Matthes et al., 2017). As the ApEEP model is now recommended as part of the solar variability forcing set in CMIP6, it is important to test the accuracy of the model output against independent data sets, as undertaken in the current study.

Nesse Tyssøy et al. (2019) concluded that the ApEEP model >30-keV fluxes are potentially too low during geomagnetic storms with Ap > 40 nT, partly because of pitch angle anisotropy within the bounce loss cone (BLC). However, Rodger et al. (2013) used satellite electron precipitation observations combined with ground-based riometer absorption to show that the BLC was isotropic during high flux EEP events, that is, indicating strong diffusion. Therefore, there is an open question about if a large geomagnetic storm will be well represented by the ApEEP model. This will depend on whether the BLC is isotropically filled by large storm-time EEP fluxes, in which case the model is likely to be correct. An updated EEP model which included eight magnetic local time (MLT) sectors was developed by van de Kamp et al. (2018), called APEEP_MLT. An important point to note is that the ApEEP model gives the same flux results as the MLT-averaged ApEEP_MLT model (van de Kamp et al., 2018). The addition of MLT sector flux information allows detailed comparison with radiation belt processes to be undertaken. In addition, it is now possible to make detailed comparison with EEP characteristics determined from ground-based subionospheric VLF narrowband radio wave observations on fixed transmitter-receiver great circle paths.

In this study, we analyze, for the first time, the impact of a large geomagnetic storm on the phase of a transmitter continuously operating over many days. VLF transmitter phase tends to be harder to measure accurately over long periods than amplitude, but it is easier to interpret. High-quality phase observations lasting almost a month are interpreted in terms of nondisturbed background ionospheric electron density profiles and storm-induced EEP fluxes. The resultant EEP fluxes are then compared with the equivalent directly observed POES >30-keV loss-cone fluxes, and the output of the ApEEP_MLT model shows where agreement exists and where discrepancies arise.

## 2. Geomagnetic Conditions and Experimental Data Sets

The time variation of the geomagnetic activity index Ap for March 2015, as well as the GOES-15 > 800-keV and > 2-MeV trapped fluxes, are shown in Figure 1. The figure shows that a large geomagnetic disturbance occurred on 17 March, with Ap exceeding 150 nT for a day, followed by a recovery over the next 4 to 5 days. The outer radiation belt fluxes at geostationary orbit ($L = 6.6$) show two to three orders of magnitude enhancements for both energy ranges associated with the geomagnetic storm, with fluxes remaining elevated, although slowly recovering, for the rest of the month (>10 days). Prior to the storm period in mid-March, geomagnetic conditions were mostly quiet, particularly from 10 to 16 March. In that time, GOES-15 fluxes were slowly subsiding toward low background levels. In this study, data from the period 14 to 16 March are used to represent pre-storm quiet day conditions.

The flux of precipitating >30-keV electrons observed in the BLC by the POES SEM-2 electron telescopes (Rodger et al., 2010) are shown for the extended study period in Figure 2. Zonal mean electron fluxes are shown for $L = 2$ to 10, with a resolution of 0.25 $L$. Enhanced fluxes at $L$-shells less than 4 are observed following the St. Patrick's Day storm on 17 March, with magnitudes reaching >$10^5$ el. $\text{cm}^{-2}\text{s}^{-1}\text{sr}^{-1}$ before slowly recovering to lower values over the next 10 days.

VLF phase data analyzed in this study were recorded by an UltraMSK receiver system (Clilverd et al., 2009) located in Reykjavik, Iceland, which was set to monitor the signals from the U.K. Naval transmitter in Skelton (22.1 kHz, call-sign GVT). The transmitter-receiver locations are shown in Figure 3. The GVT
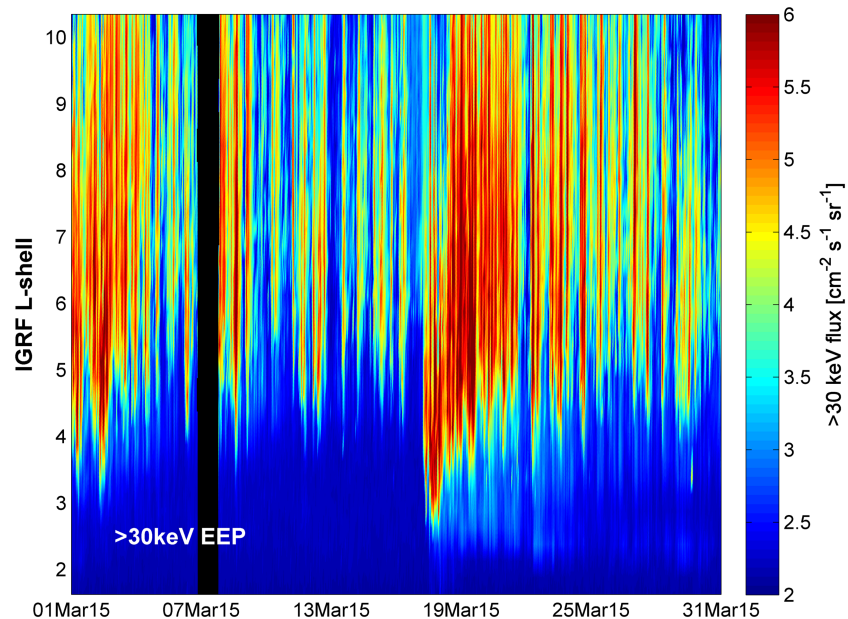
**Figure 2.** POES >30-keV zonal mean electron precipitation fluxes during march 2015 as a function of *L*-shell. Data gaps are indicated by black coloring.

transmitter location is indicated by the green circle, while the Reykjavik receiver is indicated by a red diamond. *L*-shell contours for *L* = 3.5, 4, and 5.5 are shown.

The UltraMSK software uses GPS 1PPS timing to accurately determine the relative phase of the GVT transmissions (Clilverd et al., 2009). The great circle path from Skelton to Reykjavik spans the *L*-shell range 2.7 to 5.4 and thus has the potential to be used to monitor changes in D-region ionization conditions caused by electron precipitation from the outer radiation belt. The phase analysis presented in this study is made possible because of the near-continuous operation of the GVT transmitter throughout March 2015, along with the continuous operation of the receiver. This allows relative phase variations to be determined for a period of 29 days in a row—something that is not normally possible because of instability in either transmitter phase or receiver phase-lock. The transmitter amplitude was also logged at Reykjavik; however, the amplitude levels during geomagnetic storms were highly variable and less understandable as a monitor of long-lasting perturbations, consistent with the findings of George et al. (2019) for solar flare analysis. A second receiver location is also shown in Figure 3 by a red diamond close to the transmitter, at Eskdalemuir geomagnetic observatory. The Eskdalemuir phase data is used to monitor the source transmitter phase prior to any changes induced by ionospheric perturbations.
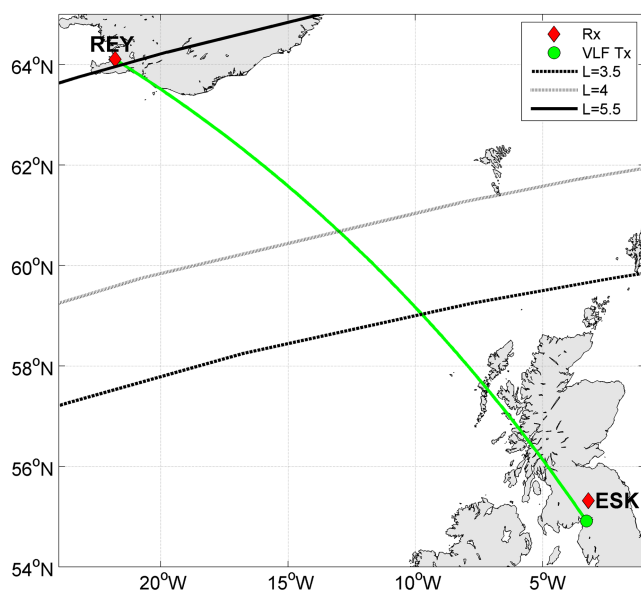


**Figure 3.** Map of the subionospheric VLF great circle propagation path from the GVT transmitter in UK (green circle) to a receiver in Reykjavik, Iceland (REY, red diamond). Also shown is the location of a complementary VLF receiver at Eskdalemuir in Scotland (ESK), which was used to verify the transmitter stability (red diamond). Geomagnetic *L*-shell contours for are shown as solid, dashed, and dotted lines.

## 3. VLF Phase Observations

The GVT transmitter typically goes off for a few hours of maintenance at the beginning of each month but otherwise remains on continuously, with high-quality phase stability for the majority of the time. The GVT relative phase variations observed from Reykjavik for March 2015 are shown in Figure 4. In the plot, a diurnal phase variation of ~170° is apparent, particularly prior to 17 March. Nighttime phase values are lower than daytime ones, with rapid transitions between the two at sunrise and sunset along the great circle path between transmitter and receiver. After the onset of enhanced geomagnetic activity on 17 March, the diurnal phase variation
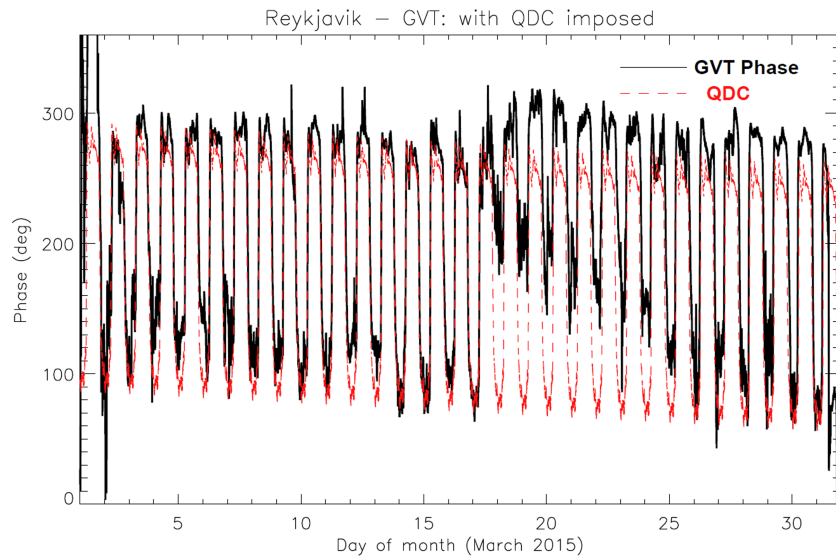
**Figure 4.** Subionospheric VLF phase in march 2015, from the UK transmitter, GVT (22.1 kHz), received at Reykjavik, Iceland (black line), with a superposed quiet-day curve (QDC, red dashed line) including a 1°/day phase drift caused by the transmitter.

patterns change significantly with higher phase values both during the day and the nighttime, effectively reducing the diurnal phase range to ~50°. We postulate that this distinct change is due to the impact of EEP on the ionosphere, affecting the subionospheric VLF radio propagation. A return to more normal diurnal phase variations can be observed toward the end of the month. Figure 4 also shows a representative quiet-day phase curve (QDC) superimposed as a red dashed line. The QDC was calculated as an average of the phase on 14, 15, and 16 March. A 1°/day phase drift was applied to the QDC throughout the month, as this was found to be a feature of the source transmissions, as determined by the AARDDVARK receiver at Eskdalemuir, which is located close to the GVT transmitter.

A more detailed plot of the pre-storm period on 16 March 2015 is shown in the upper panel of Figure 5. GVT phase variation is given by the solid black line, while the 3-day average phase variation (QDC, based on 14–16 March) is represented by the red dashed line. From 00–06 UT and 20–24 UT, the nighttime phase values are much lower than that during the daytime from 08–18 UT as expected (Thomson et al., 2007). The equivalent MLT of the midpoint of the GVT-Iceland path is given in the upper $x$-axis, and we note here that there is very little difference between UT and MLT for this path (<10 min). The superimposed diamonds indicate the phase calculated by LWPC for the GVT-Reykjavik path on 16 March, using D-region ionospheric electron number density Wait-based profiles for solar zenith angle-defined beta (sharpness) and $H'$ (reference height) values determined by McRae and Thomson (2000) and midlatitude nighttime beta and $H'$ values from Thomson and McRae (2009). Several features of note can be observed, including the sudden phase change effects of a M2 solar flare just prior to midday (see George et al., 2019 for a discussion of large solar flares and their VLF responses) and a sunrise shoulder, relative to the daytime phase levels, which is caused by ozone layer absorption of solar UV during high solar zenith angle conditions (Macotela et al., 2019). Although these two features are not captured by the LWPC modeling, the close fit between the rest of the observed phase variations, the QDC, and LWPC modeling results indicate a high-quality knowledge of the background, undisturbed ionospheric conditions prior to the geomagnetic storm on 17 March. The model-observation agreement during nighttime conditions indicates that midlatitude beta and $H'$ nighttime values can be applied to propagation paths that do not exceed 66° in latitude. This ionospheric condition knowledge provides a baseline on which to determine storm-induced phase perturbation levels and calculate the electron precipitation flux involved in generating those perturbations.

The variation in phase during the storm onset and main phase period is shown in detail in Figure 5, lower panel. The plot shows the observed phase (black line) and the QDC (red line) from 16 to 21 March 2015. Shading indicates periods of nighttime on the propagation path. Following the nondisturbed day on 16
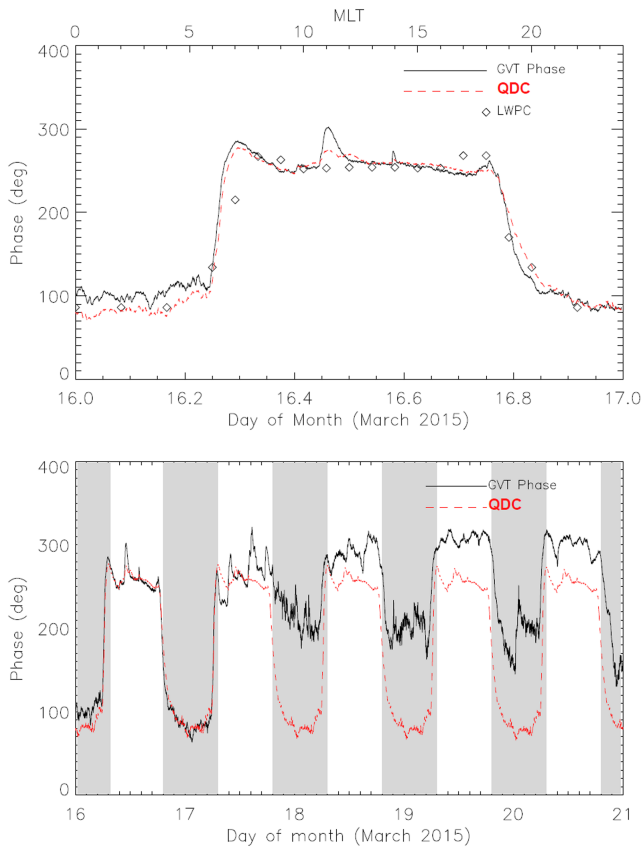
**Figure 5.** Upper panel: Diurnal variations of GVT phase received at Reykjavik (black line) on 16 march 2015, 3-day average QDC (red dashed line), and LWPC modeling results (diamonds). Lower panel: The variation of GVT phase during the first few days of the St. Patrick's day storm (black line) compared with a QDC (red). Dark shaded times indicate nighttime conditions; light shading indicates daytime on the VLF path. Substantial deviations from the QDC begin during the daytime on 17 march.
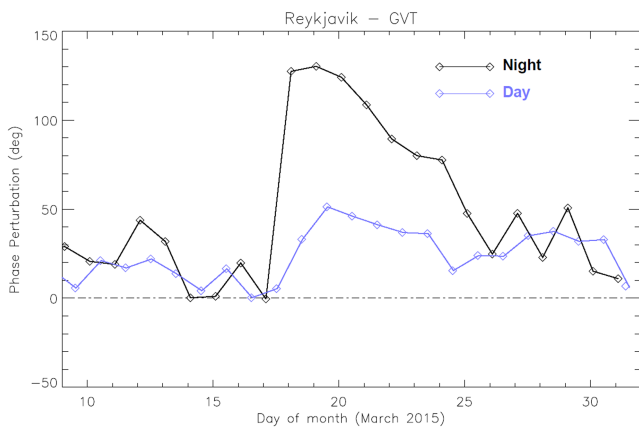


**Figure 6.** Average GVT phase perturbations during the nighttime and the daytime (night 00–05 UT black line, day 08–18 UT blue line) before and during the St. Patrick's day geomagnetic storm, which started on 17 march 2015.

March where the two lines track closely, the phase shows bursts of increased phase during the daytime of 17 March, often returning to near-QDC levels afterwards. However, during the latter part of the day when the path experiences nighttime conditions, the phase shows a consistently large phase enhancement compared with the nighttime QDC. After 17 March, the phase is continuously enhanced relative to the QDC levels during the daytime and nighttime for several days, although the nighttime values can be seen to be relaxing back toward the QDC from the start of 18 March. Daytime phase values peak on 19 March.

Average daytime (blue line) and nighttime (black line) phase perturbation levels are shown in Figure 6 for the period from 9 to 31 March 2015. The phase perturbation was calculated as the difference between the GVT phase and the QDC. The daytime values are averaged over 08–18 UT, while the nighttime values are averaged over 00–05 UT. These time ranges were selected in order to minimize the impact of rapidly changing phase during sunrise and sunset times, as seen in Figure 5. The nighttime phase perturbation value responds immediately following the start of the storm, quickly reaching peak values of ~130°, which last for 3 nights before subsiding slowly toward the zero line over the next 6 nights. Daytime phase perturbations increase steadily over 2 days, reaching a peak of ~50° before subsiding slowly for the next 5 days. After the slow recovery in nighttime and daytime phase perturbation values toward zero, from 26 March, there is an additional period of elevated phase perturbation levels. Any association with the St. Patrick's Day storm that started on 17 March is unclear.

## 4. Modeling Phase Perturbations

With knowledge of the background D-region conditions during daytime and nighttime, it is possible to calculate the levels of flux of >30-keV precipitating electrons that are required to generate the observed phase perturbations. Here, we follow the process previously described in Hardman et al. (2015), where the flux of >30-keV precipitating electrons is combined with spectral gradient information via a power law scaling exponent ($k$) in order to generate a precipitating flux from 30 to 1,000 keV. A simple chemical model is then used to determine the levels of excess ionization generated over a range of altitudes from 50–100 km. Finally, the resultant electron number density profiles are input into the LWPC subionospheric propagation model in order to calculate the expected phase changes for a given transmitter and receiver path. A full description of this process is given in Rodger et al. (2012) and Simon Wedlund et al. (2014). As the D-region has higher electron number densities at low altitude during the daytime, compared with the nighttime, the same precipitation flux will produce different electron number density profiles at these times, and therefore different radio wave perturbation levels.

We want to invert the process described above to calculate the flux of >30-keV electrons from the phase perturbation. In order to undertake this calculation for the St. Patrick's Day storm of March 2015, we use the ambient ionospheric conditions for daytime and nighttime prior to the storm obtained using the Wait profile as described in section 3, and the levels of phase perturbation observed on the GVT-Reykjavik subionospheric propagation path for each day and night during the storm. However, we have no ground-based experimental information that would allow us to determine the spectral gradient ($k$), and therefore, we use the results from a comprehensive analysis of DEMETER electron flux observations, which
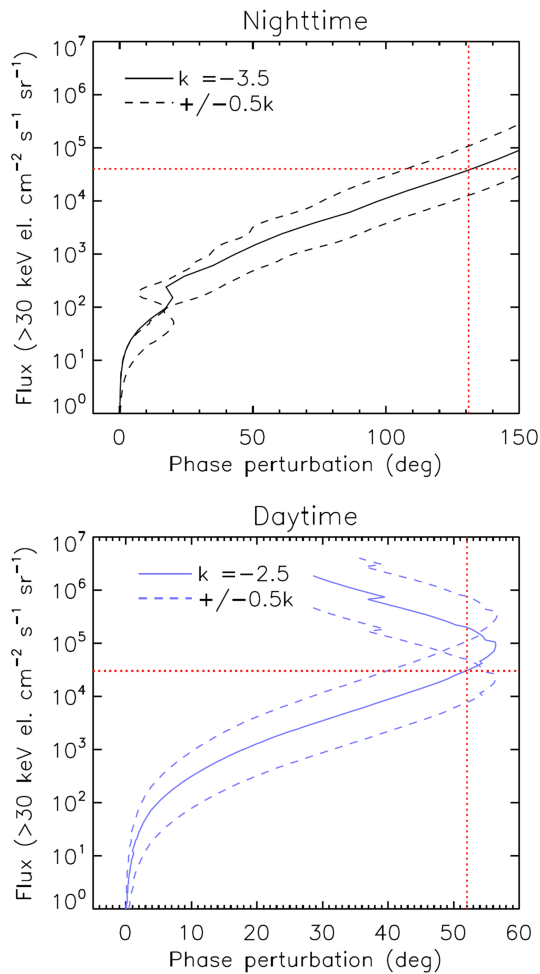
**Figure 7.** Modeled GVT phase perturbation variation with >30-keV electron precipitation flux for nighttime D-region conditions (upper panel) and daytime conditions (lower panel). Solid lines represent electron energy power law spectral gradient $k = -3.5$, while dashed lines represent $\Delta k = \pm 0.5$. Red dotted lines indicate the maximum phase perturbation level observed during the St. Patrick's day storm. See text for more details.

indicate that $k \sim -3$ for outer radiation belt fluxes during quiet geomagnetic conditions, and $k \approx -3.5$ for moderate/high disturbed conditions (see figure 8 in Whittaker et al., 2013). A similar power law spectral gradient analysis has also been undertaken for POES SEM-2 electron flux data (van de Kamp et al., 2016; 2018) identifying similar gradient values over a wide range of geomagnetic activity levels with median $k$ ranging from $-3$ to $-4$ during nighttime and $-2$ to $-3$ during the daytime, particularly for outer radiation belt fluxes where $L < 5.5$, as in this study (see figure 3 in van de Kamp et al., 2018). However, this study does not use the van de Kamp results directly because they are already included in the ApEEP model being investigated here.

The variation of the level of phase perturbation with imposed electron precipitation flux >30 keV is shown in Figure 7, with the upper panel representing nighttime results and the lower panel representing that of daytime. The nighttime panel shows phase perturbation variations for a $k = -3.5$ power law spectrum (solid black line) and for $k = -3$ and $k = -4$ (dashed lines). A vertical dotted line indicates the maximum phase perturbation level, which was achieved on 19 March as shown in Figure 6. A horizontal red dotted line highlights the $k = -3.5$ flux level for the 131° peak nighttime perturbation, suggesting a peak nighttime flux of $4 \times 10^4$ el. cm$^{-2}$ sr$^{-1}$ s$^{-1}$ with an uncertainty of a factor of 3 above and below, introduced by the $k = -3$ to $-4$ range. The panel shows that the phase perturbation levels increase smoothly with increasing flux levels, and therefore, during nighttime, the phase perturbation is a good indicator of precipitating flux levels. However, because of the combined effect of path length and electron density on the received phase, the relation between flux and phase is not always necessarily linear. The daytime panel shows the phase perturbation variations for a $k = -2.5$ power law spectrum (solid blue line), with $k = -2$ and $k = -3$ results shown as dashed blue lines. The vertical dotted line indicates the maximum observed phase perturbation level (52°), intersecting the $k = -2.5$ line at the horizontal red dotted line given by a flux level of $3 \times 10^4$ el. cm$^{-2}$ sr$^{-1}$ s$^{-1}$. However, the daytime phase perturbations levels show a maximum effect of $\sim 55°$ before reducing as higher precipitating electron fluxes are applied, leading to two possible flux level results for a single-phase perturbation value. This leads to a much larger uncertainty in the flux, possibly as much as two orders of magnitude.

The daytime overturning phase issue potentially explains the relatively low perturbation level determined on 18 March compared with that on 19 March (34° c.f. 52°; see Figure 6). Figure 7 suggests that instead of moderate $\sim 10^4$ el. cm$^{-2}$ sr$^{-1}$ s$^{-1}$ flux levels generating the 34° daytime perturbation, it could be that there are much higher fluxes involved, possibly $\sim 10^6$ el. cm$^{-2}$ sr$^{-1}$ s$^{-1}$. Clearly, these overturning daytime phase perturbation levels can lead to large uncertainties in any estimated flux levels for those time periods, despite the well-resolved phase changes that were observed during the storm. Error bars on VLF-phase-derived fluxes shown later in the study take this uncertainty into account.

## 5. Flux Comparisons

Having determined the response of the GVT-Reykjavik path to electron precipitation fluxes, we can invert this relation to convert the observed phase perturbations into an estimate of the >30-keV precipitation flux during the 2015 St. Patrick's Day storm period. Comparison of the fluxes can be made against the electron precipitation model, ApEEP, recently published with MLT included (van de Kamp et al., 2018), which can provide fluxes in the region of the GVT-Reykjavik path by using the appropriate MLT zone as MLT varies through the day at the longitude of the subionospheric propagation path. A further comparison can be
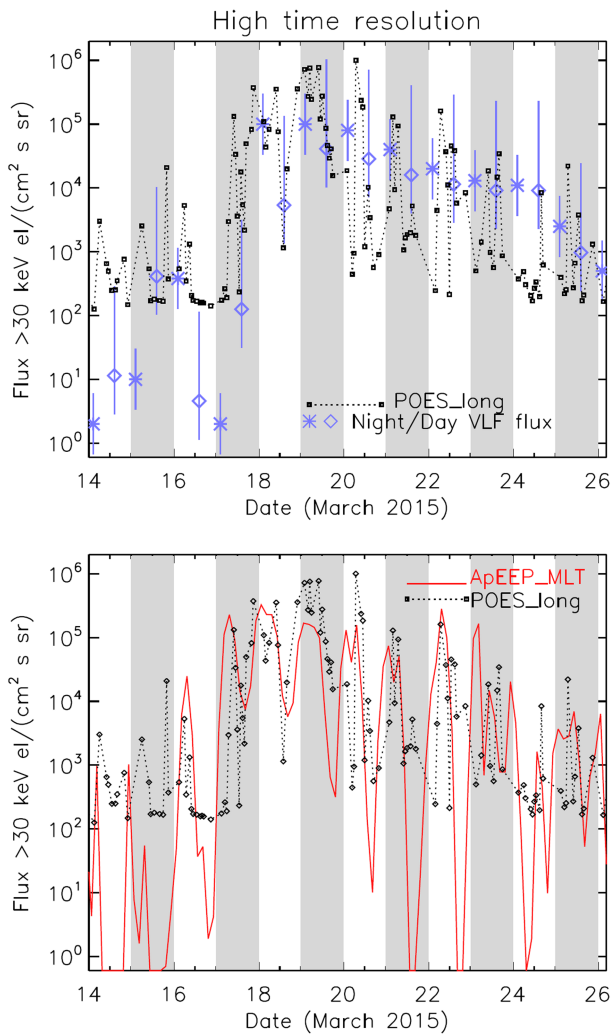
**Figure 8.** Upper panel: The >30-keV flux determined using the VLF phase measurements during the St. Patrick's day storm of march 2015 (blue asterisks, night; blue diamonds, day). Vertical lines indicate uncertainty ranges. The black dashed line shows the POES >30-keV flux levels determined from the 0° electron telescope with a 3-hourly resolution in the longitude range 30°W to 15°E, averaged over the $L$-shell range $L = 2.64$ to 5.44. Lower panel: The ApEEP_MLT model output (red line) for the MLT range equivalent to the Scotland-Iceland VLF path and the POES >30-keV flux levels in the longitude range 30°W to 15°E. see text for more details. Alternate days are shaded for clarity.

made against the POES SEM-2 fluxes (Rodger et al., 2010) measured in the longitude region encompassing the GVT-Reykjavik path.

The upper panel of Figure 8 shows the time-varying >30-keV flux determined using the VLF phase measurements during the St. Patrick's Day storm of March 2015. Nighttime flux levels are indicated by blue asterisks, and daytime levels by blue diamonds. Vertical lines indicate uncertainty ranges generated by $\pm 0.5\ k$ (see Figure 7). The directly observed POES >30-keV flux levels determined from the 0° electron telescope with a 3-hourly resolution in the longitude range 30° W to 15° E, averaged over the $L$-shell range $L = 2.64$ to 5.44, is indicated by the black dashed line. Initially, the VLF phase-derived fluxes are substantially lower than the POES fluxes, which is primarily due to the POES SEM-2 instrument measurement noise floor of $10^2$ el. $cm^{-2}\ sr^{-1}\ s^{-1}$ (Rodger et al., 2010), limiting the ability of the satellite instrument to detect quiet- or low-level precipitation fluxes. However, during the storm, there is good agreement between the VLF phase fluxes and the POES fluxes, both during the day and the night, particularly when taking into account the error bars in the VLF flux. However, there are some POES flux values that are lower than the VLF-inferred fluxes, particularly after 20 March. This may be caused by substantial flux variations occurring over small distance scales, which the long-wavelength VLF technique is relatively insensitive to, but do influence the POES values. This would suggest that small-scale precipitation structure is a feature of the recovery phase of this geomagnetic storm period.

The lower panel of Figure 8 shows a comparison between the ApEEP_MLT model output (red line) and the directly observed POES >30-keV flux levels determined from the 0° electron telescope with a 3-hourly resolution in the longitude range 30°W to 15°E, averaged over the $L$-shell range $L = 2.64$ to 5.44 (black dashed line). Reasonable agreement between the model and the POES observations occurs during the storm period, including peak flux levels, and in the temporal variations throughout each day during the main phase of the storm. During the recovery phase of the storm, that is, after 20 March 2015, the ApEEP_MLT model shows a large range of flux, with very low fluxes repeating quasi-daily in the late afternoon (in both UT and MLT). This is caused by much lower electron precipitation fluxes occurring in the MLT afternoon sector in the observations used to build the model, potentially due to the lack of whistler-mode chorus waves in this MLT sector (e.g., see figure 7 of Summers et al., 1998). Prior to the onset of the St. Patrick's Day storm, the POES >30-keV fluxes tend to hover around the SEM-2 instrument measurement noise floor of $10^2$ el. $cm^{-2}\ sr^{-1}\ s^{-1}$ (Rodger et al., 2010),

while the ApEEP_MLT model is significantly lower, showing more agreement with the VLF phase results shown in the upper panel.

## 6. Validation

Subionospheric VLF phase measurements of the UK transmitter, GVT, made from Reykjavik, Iceland, were highly reliable over almost the whole month of March 2015. The reliability of the phase measurements has allowed a derivation of the EEP fluxes generated throughout the St. Patrick's Day geomagnetic storm. Daytime and nighttime electron precipitation flux derivations are made, taking into account differing background D-region conditions upon which the electron precipitation generates excess ionization. The electron precipitation flux (>30 keV) derived from VLF measurements can be compared with equivalent directly observed POES satellite fluxes and the ApEEP_MLT model. In all three data series, the St. Patrick's Day
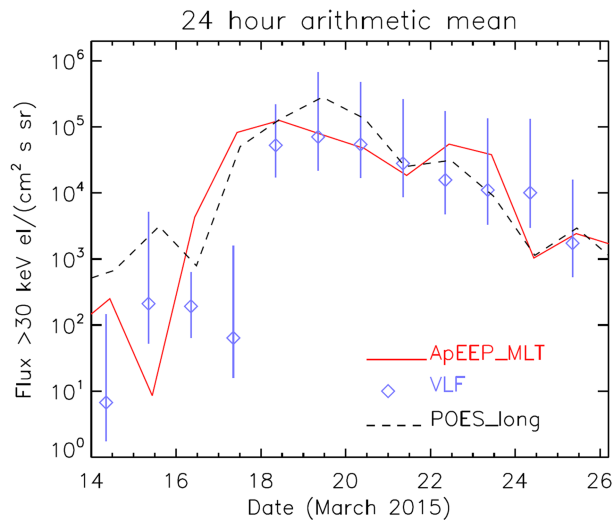
**Figure 9.** 24-hr average >30-keV electron precipitation fluxes determined using the ApEEP_MLT predictive flux model (red line), VLF phase perturbations (blue diamonds), and the longitudinally restricted POES >30-keV measurements (black dashed line). VLF uncertainty ranges were calculated using an average of the day and nighttime uncertainty ranges shown in Figure 8.

storm generated large electron precipitation fluxes, with the highest levels observed during the night and the highest variability observed during the day (UT and MLT).

An important question associated with the ApEEP_MLT model is about its applicability for use in coupled-climate model runs (Matthes et al., 2017, van de Kamp et al., 2018). Are the ApEEP-predicted fluxes correct, and does the model capture the dynamics of electron precipitation from large geomagnetic storms properly? The CMIP6 solar forcing data set containing the ApEEP model output provides daily average flux descriptions for input into climate models (Matthes et al., 2017). Thus, in order to appropriately compare the VLF-derived fluxes, POES fluxes at the longitude of the Iceland-UK VLF propagation path, and the ApEEP model-predicted fluxes with appropriate MLT output for the same longitude region, an analysis of daily average fluxes is undertaken here.

Nesse Tyssøy et al. (2019) concluded that the CMIP6 >30-keV fluxes are potentially underrepresented during geomagnetic storms with large Ap and provide a general underestimate because of the limitations of the POES electron precipitation telescope (Nesse Tyssøy et al., 2016). We note that the ApEEP model-predicted fluxes used in CMIP6 analysis does not include any MLT variability, while the ApEEP_MLT does. In our study, the MLT version of the ApEEP model is required in order to compare against the specific VLF propagation path analyzed. However, van de Kamp et al. (2018) showed that the ApEEP_MLT model-predicted fluxes, when zonally averaged, generated fluxes equivalent to that of the non-MLT model used in CMIP6, so we can assume the conclusions of Nesse Tyssøy et al. (2019) to also be valid for the ApEEP_MLT model-predicted fluxes.

Figure 9 shows 24-hr average >30-keV electron precipitation fluxes determined using the ApEEP_MLT model, VLF phase perturbations, and the longitudinally restricted POES >30-keV measurements. VLF uncertainty ranges were calculated using an average of the day and nighttime uncertainty ranges shown in Figure 8. All averages are undertaken as an arithmetic mean. We note that somewhat different values could be obtained if other averaging methods are used. The plot shows that at about the time of the geomagnetic storm (19 March 2015), the electron precipitation fluxes determined from the VLF phase perturbations and the POES satellite show good agreement. This is consistent with strong diffusion conditions filling the BLC isotropically (Kennel & Petschek, 1966), leading to POES 0° telescope fluxes providing an accurate measurement of the precipitation flux (Nesse Tyssøy et al., 2016; Rodger et al., 2013). During the recovery phase of the storm period (20–26 March), the POES electron precipitation fluxes show a steady decline, which is also mirrored by the fluxes determined from the VLF phase perturbations. Differences between the 24-hr average POES measurements and the 24-hr average VLF phase calculations during the storm (i.e., from 18 to 25 March) are only a factor of 1.3, which might suggest that any influence of nonisotropic flux distributions within the BLC (Nesse Tyssøy et al., 2016; Rodger et al., 2013) is masked by spectral gradient uncertainties as discussed above.

The ApEEP_MLT model is based on POES electron precipitation measurements organized by the geomagnetic index Ap, and so some agreement is expected between the model-predicted fluxes and the POES longitudinally restricted measurements during this study period (van de Kamp et al., 2018). The ApEEP_MLT model does a good job of capturing the overall time variation of the storm-induced electron precipitation fluxes and more realistically exhibits a lower noise floor prior to the storm than reported by the POES fluxes. The ApEEP_MLT model storm-time fluxes are only about a factor of 1.7 lower than the POES fluxes. Since the ApEEP_MLT model was based on average values, it would be expected to produce higher fluxes than POES for some geomagnetic storms and lower for some others. However, the close agreement in >30-keV flux levels during the St. Patrick's Day storm, using the three different techniques shown here, is encouraging for long model simulation runs (e.g., decadal climate simulations, (Matthes et al., 2017)) for which the ApEEP model was created.

Comparison of the ApEEP_MLT model with the fluxes determined from VLF phase perturbations is made difficult because of the uncertainty in the energy spectral gradient of the electron precipitation. Is the difference in flux during the St. Patrick's Day storm due to statistical variability between the model and the VLF phase technique, or due to uncertainty in the energy spectral gradient of the electron precipitation, or due to nonisotropic BLC distribution effects on POES measurements (and therefore the ApEEP_MLT model)? We could use POES measurements to calculate the energy spectral gradient of the precipitating electrons or use the information provided in the ApEEP_MLT model (van der Kamp et al., 2016; 2018). However, there is the potential for any errors in flux level determination using nonisotropic POES measurements to also influence equivalent estimates of energy spectral gradient. In addition, using extra information originating from one of the data sets would compromise the independence of the comparison. Thus, it is clearly more reasonable to determine the energy spectral gradients independently, which we have attempted here using DEMETER electron measurements.

## 7. Summary

Subionospheric VLF transmitter phase measurements have been used to infer the >30-keV electron precipitation flux generated from the outer radiation belt, $L < 5.5$, during the St. Patrick's Day storm of March 2015. Measurements made close to the transmitter (at Eskdalemuir in Scotland) showed that the transmitted phase was constant, apart from a 1° a day systematic drift, allowing more distant observations to be used to determine phase perturbations due to electron precipitation flux. Enhanced >30-keV electron precipitation fluxes lasted for 8 days, with peak fluxes during the main phase of the storm three to four orders of magnitude higher than pre-storm levels, followed by a slow recovery thereafter. During the extended storm period, comparison between VLF-inferred >30-keV electron precipitation fluxes, directly observed POES >30-keV 0° telescope fluxes, and the CMIP6 >30-keV electron precipitation flux prediction model shows that

1. VLF-inferred >30-keV fluxes are similar to the equivalent POES fluxes during the storm, suggesting a weak or masked effect of non-isotropic pitch angle distributions in the BLC, particularly during high flux precipitation (Rodger et al., 2013).
2. The directly observed POES >30-keV fluxes are typically a factor of only 1.7 higher than the CMIP6 model-predicted fluxes, primarily due to higher storm-generated flux levels during the daytime.
3. CMIP6 >30-keV predicted fluxes for $L < 5.5$ are of the same order of magnitude as the VLF-inferred >30-keV fluxes in the pre-storm period, and typically one to two orders of magnitude lower than the observed POES pre-storm fluxes.

The analysis presented here provides a detailed comparison between satellite >30-keV electron precipitation flux measurements, VLF phase-inferred fluxes, and the CMIP6 predictive flux model during one large geomagnetic storm. The finding that the CMIP6 model of predicted electron precipitation (ApEEP) underrepresents geomagnetic storm-time fluxes is consistent with previous analysis undertaken by Nesse Tyssøy et al. (2019), although the underestimate is found to be small. Realistic electron precipitation fluxes, as inferred from VLF signal analysis and POES observations during the storm, could be as large as a factor of 1.7 higher than currently estimated by the ApEEP predictive model (Matthes et al., 2017). The atmospheric impact of these higher flux levels in the medium energy range (i.e., 30–1000 keV) needs to be investigated further. Following the conclusions of this study, the use of the CMIP6 model of predicted electron precipitation (ApEEP) is appropriate in terms of estimating electron precipitation flux variations during geomagnetic storms. The comparison done in this study used the MLT version of ApEEP rather than the zonally averaged version used in the CMIP6 data set. However, we note that the MLT version, when zonally averaged, was found to be equivalent to the ApEEP version used in the CMIP6 data set, but with lower quiet-time fluxes. For shorter time period runs that are made during the POES observational period, we recommend using EEP from the direct POES measurements. A detailed description of these data sets can be found at http://chamos.fmi.fi/chamos_apeep.html.

## References

Andersson, M., Verronen, P. T., Marsh, D. R., Seppälä, A., Päivärinta, S.-M., Rodger, C. J., et al. (2018). Polar ozone response to energetic particle precipitation over decadal time scales: The role of medium-energy electrons. *Journal of Geophysical Research*, *123*, 607–622. https://doi.org/10.1002/2017JD027605

Andersson, M., Verronen, P. T., Rodger, C. J., Clilverd, M. A., & Seppälä, A. (2014). Missing driver in the sun–earth connection from energetic electron precipitation impacts mesospheric ozone. *Nature Communications*, 5. https://doi.org/10.1038/ncomms6197

Baker, D. N., Jaynes, A. N., Kanekal, S. G., Foster, J. C., Erickson, P. J., Fennell, J. F., & Henderson, M. G. (2016). Highly relativistic radiation belt electron acceleration, transport, and loss: Large solar storm events of march and June 2015. *Journal of Geophysical Research: Space Physics*, 121(7), 6647–6660. https://doi.org/10.1002/2016JA022502

Brasseur, G., & Solomon, S. (2005). *Aeronomy of the Middle Atmosphere: Chemistry and Physics of the Stratosphere and Mesosphere*, (3rd ed.). Dordrecht: Springer.

Clilverd, M A, C J Rodger, M Andersson, P T Verronen, and A Seppälä (2016). Linkages between the radiation belts, polar atmosphere and climate: Electron precipitation through wave particle interactions. In *Waves, particles and storms in geospace*, edited by I. Mann et al., Chapter 14, 355-376, Oxford University Press, https://doi.org/10.1093/acprof:oso/9780198705246.003.0015, ISBN: 9780198705246.

Clilverd, M. A., Rodger, C. J., Gamble, R. J., Th, U., Raita, T., Seppälä, A., et al. (2010). Ground-based estimates of outer radiation belt energetic electron precipitation fluxes into the atmosphere. *Journal of Geophysical Research*, 115, A12304. https://doi.org/10.1029/2010JA015638

Clilverd, M. A., et al. (2009). Remote sensing space weather events: Antarctic-Arctic radiation-belt (dynamic) deposition-VLF atmospheric research Konsortium network. *Space Weather*, 7, S04001. https://doi.org/10.1029/2008SW000412

Ferguson, J. A., & Snyder, F. P. (1990). *Computer Programs for Assessment of Long Wavelength Radio Communications, Version 1.0: Full FORTRAN Code user's Guide, Naval Ocean Systems Center Tech. Doc. 1773, DTIC AD-B144 839*. Alexandria, Va: Def. Tech. Inf. Cent.

George, H., Rodger, C. J., Clilverd, M. A., Cresswell-Moorcock, K., Brundell, J. B., & Thomson, N. R. (2019). Developing a nowcasting capability for X-class solar flares using radiowave propagation changes. *Space Weather*. https://doi.org/10.1029/2019SW002297

Glauert, S. A., Horne, R. B., & Meredith, N. P. (2018). A 30-year simulation of the outer electron radiation belt. *Space Weather*, 16, 1498–1522. https://doi.org/10.1029/2018SW001981

Gokani, S. A., Kosch, M., Clilverd, M. A., Rodger, C. J., & Sinha, A. K. (2019). What fraction of the outer radiation belt relativistic electron flux at $L \approx 3$–4.5 was lost to the atmosphere during the dropout event of the St Patrick's day storm of 2015. *Journal of Geophysical Research*, 124. https://doi.org/10.1002/2018JA026278

Hardman, R., Clilverd, M. A., Rodger, C. J., Brundell, J. B., Duthie, R., Holzworth, R. H., et al. (2015). A case study of electron precipitation fluxes due to plasmaspheric hiss. *Journal of Geophysical Research*, 120, 6736–6748. https://doi.org/10.1002/2015JA021429

Hendry, A. T., Rodger, C. J., & Clilverd, M. A. (2017). Evidence of sub-MeV EMIC-driven electron precipitation. *Geophysical Research Letters*, 44, 1210–1218. https://doi.org/10.1002/2016GL071807

Horne, R. B., Meredith, N. P., Glauert, S. A., & Kersten, T.(2016). Wave driven diffusion in radiation belt dynamics. In *Waves, Particles, and Storms in Geospace: A Complex Interplay* (pp. 217–243). Oxford: Oxford University Press.

Kennel, C. F., & Petschek, H. E. (1966). Limit on stably trapped particle fluxes. *Journal of Geophysical Research*, 71(1), 1–28. https://doi.org/10.1029/JZ071i001p00001

Macotela, E. L., Clilverd, M. A., Manninen, J., Thomson, N. R., Newnham, D. A., & Raita, T. (2019). The effect of ozone shadowing on the D region ionosphere during sunrise. *Journal of Geophysical Research*, 124, 3729–3742. https://doi.org/10.1029/2018JA026415

Matthes, K. B., Funke, M. E., Andersson, L., Barnard, Beer, J., et al. (2017). Solar forcing for CMIP6 (v3.2). *Geoscientific Model Development*, 10, 2247-2302. https://doi.org/10.5194/gmd-10-2247-2017

Maurya, A., Venkatesham, K., Kumar, S., Singh, R., Tiwari, P., & Singh, A. (2018). *Effects of St. Patrick's Day Geomagnetic Storm of March 2015 and of June 2015 on Low-Equatorial D Region Ionosphere*. Journal of Geophysical Research: Space Physics. https://doi.org/10.1029/2018JA025536

McRae, W. M., & Thomson, N. R. (2000). VLF phase and amplitude: Daytime ionospheric parameters. *Journal of Atmospheric and Solar - Terrestrial Physics*, 62(7), 609–618.

Meredith, N. P., Horne, R. B., Clilverd, M. A., Horsfall, D., Thorne, R. M., & Anderson, R. R. (2006). Origins of plasmaspheric hiss. *Journal of Geophysical Research*, 111, A09217.

Neal, J. J., Rodger, C. J., Clilverd, M. A., Thomson, N. R., Raita, T., & Ulich, T. (2015). Long-term determination of energetic electron precipitation into the atmosphere from AARDDVARK subionospheric VLF observations. *Journal of Geophysical Research*, 120, 2194–2211. https://doi.org/10.1002/2014JA020689

Nesse Tyssøy, H., Haderlein, A., Sandanger, M., & Stadsnes, J. (2019). Intercomparison of the POES/MEPED loss cone electron fluxes with the CMIP6 parametrization. *Journal of Geophysical Research: Space Physics*, 124, 628–642. https://doi.org/10.1029/2018JA025745

Nesse Tyssøy, H., Sandanger, M. I., Ødegaard, L.-K. G., Stadsnes, J., Aasnes, A., & Zawedde, A. E. (2016). Energetic electron precipitation into the middle atmosphere—Constructing the loss cone fluxes from MEPED POES. *Journal of Geophysical Research: Space Physics*, 121, 5693–5707.

Newnham, D. A., Clilverd, M. A., Rodger, C. J., Hendrickx, K., Megner, L., Kavanagh, A. J., et al. (2018). Observations and modelling of increased nitric oxide in the Antarctic polar middle atmosphere associated with geomagnetic storm driven energetic electron precipitation. *Journal of Geophysical Research*, 123, 6009–6025. https://doi.org/10.1002/2018JA025507

O'Brien, T. P., Lorentzen, K. R., Mann, I. R., Meredith, N. P., Blake, J. B., Fennell, J. F., et al. (2003). Energization of relativistic electrons in the presence of ULF power and MeV microbursts: Evidence for dual ULF and VLF acceleration. *Journal of Geophysical Research*, 108(A8), 1329. https://doi.org/10.1029/2002JA009784

Orsolini, Y. J., Smith-Johnsen, C., Marsh, D. R., Stordal, F., Rodger, C. J., Verronen, P. T., & Clilverd, M. A. (2018). Mesospheric nitric acid enhancements during energetic electron precipitation events simulated by WACCM-D. *Journal of Geophysical Research*, 123, 6984–6998. https://doi.org/10.1029/2017JA025002

Reeves, G. D., McAdams, K. L., Friedel, R. H. W., & O'Brien, T. P. (2003). Acceleration and loss of relativistic electrons during geomagnetic storms. *Geophysical Research Letters*, 30(10). https://doi.org/10.1029/2002GL016513

Rodger, C. J., Clilverd, M. A., Green, J., & Lam, M.-M. (2010). Use of POES SEM-2 observations to examine radiation belt dynamics and energetic electron precipitation in to the atmosphere. *Journal of Geophysical Research*, 115, A04202. https://doi.org/10.1029/2008JA014023

Rodger, C. J., Clilverd, M. A., Kavanagh, A. J., Watt, C. E. J., Verronen, P. T., & Raita, T. (2012). Contrasting the responses of three different ground-based instruments to energetic electron precipitation. *Radio Science*, 47(2), RS2021. https://doi.org/10.1029/2011RS00497

Rodger, C. J., Clilverd, M. A., Thomson, N. R., Gamble, R. J., Seppälä, A., Turunen, E., et al. (2007). Radiation belt electron precipitation into the atmosphere: Recovery from a geomagnetic storm. *Journal of Geophysical Research*, 112, A11307. https://doi.org/10.1029/2007JA012383

Rodger, C. J., Kavanagh, A. J., Clilverd, M. A., & Marple, S. R. (2013). Comparison between POES energetic electron precipitation observations and riometer absorptions: Implications for determining true precipitation fluxes, J. Geophys. Res. *Space Physics*, *118*, 7810–7821. https://doi.org/10.1002/2013JA019439

Seppälä, A., & Clilverd, M. A. (2014). Energetic particle forcing of the northern hemisphere winter stratosphere: Comparison to solar irradiance forcing. *Frontiers in Physics*, *2*(25), 6. https://doi.org/10.3389/fphy.2014.00025

Seppälä, A., Randall, C. E., Clilverd, M. A., Rozanov, E., & Rodger, C. J. (2009). Geomagnetic activity and polar surface level air temperature variability. *Journal of Geophysical Research*, *114*, A10312. https://doi.org/10.1029/2008JA014029

Shprits, Y. Y., Kellerman, A., Aseev, N., Drozdov, A. Y., & Michaelis, I. (2017). Multi-MeV electron loss in the heart of the radiation belts. *Geophysical Research Letters*, *44*(3), 1204–1209. https://doi.org/10.1002/2016GL072258

Simon Wedlund, M., Clilverd, M. A., Rodger, C. J., Cresswell-Moorcock, K., Cobbett, N., Breen, P., et al. (2014). A statistical approach to determining energetic outer radiation-belt electron precipitation fluxes. *Journal of Geophysical Research*, *119*, 3961–3978. https://doi.org/10.1002/2013JA019715

Summers, D., Thorne, R. M., & Xiao, F. (1998). Relativistic theory of wave-particle resonant diffusion with application to electron acceleration in the magnetosphere. *Journal of Geophysical Research: Space Physics*, *103*(A9), 20,487–20,500.

Thomson, N. R., Clilverd, M. A., & McRae, W. M. (2007). Nighttime ionospheric D region parameters from VLF phase and amplitude. *Journal of Geophysical Research*, *112*, A07304. https://doi.org/10.1029/2007JA012271

Thomson, N. R., Clilverd, M. A., & Rodger, C. J. (2014). Low latitude ionospheric D-region dependence on solar zenith angle. *Journal of Geophysical Research*, *119*, 6865–6875. https://doi.org/10.1002/2014JA020299

Thomson, N. R., Clilverd, M. A., & Rodger, C. J. (2017). Midlatitude ionospheric D region: Height, sharpness and solar zenith angle. *Journal of Geophysical Research*, *122*, 8933–8946. https://doi.org/10.1029/2017JA024455

Thomson, N. R., Clilverd, M. A., & Rodger, C. J. (2018). Quiet daytime Arctic ionospheric D region. *Journal of Geophysical Research*, *123*, 9726–9742. https://doi.org/10.1002/2018JA025669

Thomson, N. R., & McRae, W. M. (2009). Nighttime ionospheric D region: Equatorial and non-equatorial. *Journal of Geophysical Research*, *114*, A08305. https://doi.org/10.1029/2008JA014001

van de Kamp, M., Rodger, C. J., Seppälä, A., Clilverd, M. A., & Verronen, P. T. (2018). An updated model providing long-term datasets of energetic electron precipitation, including zonal dependence. *Journal of Geophysical Research*, *123*, 9891–9915. https://doi.org/10.1029/2017JD028253

van de Kamp, M., Seppälä, A., Clilverd, M. A., Rodger, C. J., Verronen, P. T., & Whittaker, I. (2016). A model providing long-term datasets of energetic electron precipitation during geomagnetic storms. *Journal of Geophysical Research*, *121*, 12,520–12,540. https://doi.org/10.1002/2015JD024212

Verronen, P. T., Seppälä, A., Clilverd, M. A., Rodger, C. J., Kyrölä, E., Enell, C.-F., et al. (2005). Diurnal variation of ozone depletion during the October–November 2003 solar proton events. *Journal of Geophysical Research*, *110*, A09S32. https://doi.org/10.1029/2004JA010932

Wait, J. R., & Spies, K. P. (1964). Characteristics of the earth-ionosphere waveguide for VLF radio waves, NBS tech. In *Note 300* (Chap. 2, p. 5). Natl. Bur. of Stand.: Boulder, Colo.

Whittaker, I. C., Gamble, R. J., Rodger, C. J., Clilverd, M. A., & Sauvaud, J. A. (2013). Determining the spectra of radiation belt electron losses: Fitting DEMETER instrument for detecting particle observations for typical and storm-times. *Journal of Geophysical Research*, *118*. https://doi.org/10.1002/2013JA019228

Wu, C-C., Liou, K., Lepping, R.P., Hutting, L., Plunkett, S., Howard, R. A., & Socker, D. (2016). The first super geomagnetic storm of solar cycle 24: "The St. Patrick's Day event (17 March 2015)", Earth, Planets and Space, 68, 1.